International Journal of Greenhouse Gas Control 22 (2014) 1–14

Contents lists available at ScienceDirect

International Journal of Greenhouse Gas Control

journal homepage: www.elsevier.com/locate/ijggc

Pore-scale imaging of trapped supercritical carbon dioxide in sandstones and carbonates

Matthew Andrew*, Branko Bijeljic, Martin J. Blunt

Department of Earth Science and Engineering, Imperial College London, United Kingdom

ARTICLE INFO

Article history:
Received 13 October 2013
Received in revised form
20 December 2013
Accepted 23 December 2013
Available online 20 January 2014

Keywords:
Carbon capture and storage
Pore-scale
Reservoir condition
X-ray microtomography

ABSTRACT

Geological carbon dioxide storage must be designed such that the CO_2 cannot escape from the rock formation into which it is injected, and often simple stratigraphic trapping is insufficient. CO_2 can be trapped in the pore space as droplets surrounded by water through capillary trapping. X-ray microtomography was used to image, at a resolution of 6.6 μm, the pore-scale arrangement of these droplets in three carbonates and two sandstones. The pressures and temperatures in the pore space were representative of typical storage formations, while chemical equilibrium was maintained between the CO_2, brine and rock phases to replicate conditions far away from the injection site. In each sample substantial amounts of CO_2 were trapped, with the efficiency of trapping being insensitive to pore-morphology and chemistry. Apart from in one extremely well connected sample, the size distribution of residual ganglia larger than 10^5 voxel^3 obey power law distributions with exponents broadly consistent with percolation theory over two orders of magnitude. This work shows that residual trapping can be used to locally immobilise CO_2 in a wide range of rock types.

1. Introduction

Carbon capture and storage (CCS) is the process where CO_2 is captured from large point sources and stored, normally in porous rock, displacing resident brine, oil or gas, such that the CO_2 remains underground for hundreds to thousands of years. The four principal mechanisms available to immobilise CO_2 on these time scales are stratigraphic, solubility, mineral and residual trapping. Stratigraphic trapping is where CO_2 is immobilised underneath impermeable boundary rocks; solubility trapping is where CO_2 dissolves into the brine surrounding the CO_2 plume (Ennis-King and Paterson, 2002); mineral trapping is where solid carbonate mineral phases are precipitated into the pore-space of the rock (Lin et al., 2007); and residual or capillary trapping is where CO_2 is held by surface forces as tiny droplets (ganglia) in the pore-space of the rock. This is the only rapid mechanism that occurs when water invades the pore-space after the injection of CO_2 – it can occur either naturally, by the migration of the CO_2 plume, or can be induced by the injection of chase brines (Qi et al., 2009).

Carbonate and sandstone saline aquifers represent important potential storage sites for CO_2 due to their large capacities and wide geographical spread. In these aquifers the injected CO_2 would reside as a dense super critical phase ($scCO_2$), increasing storage capacities. Aquifers are, however, associated with uncertainties in storage security due to potential seismic instability and leakage through abandoned wells. Also the seal integrity is less certain than for depleted oil and gas reservoirs, where effective seals have already been proven (Hawkes et al., 2005; IPCC, 2007; Lackner, 2003). In these situations trapping methods other than simple stratigraphic trapping become extremely attractive, particularly residual trapping over the short to medium term (Bachu, 2008). Therefore, it is of great importance to find the saturation of $scCO_2$ from capillary trapping in natural rock, as well as its distribution in the pore space, since this controls the longer-term processes, dissolution and mineralisation.

X-ray microtomography (μCT) has developed as a technique over the last 25 years from early attempts to visualise both dry geological samples (Flannery et al., 1987) and multiple fluid phases (Jatsi et al., 1993) to the primary method for the non-invasive imaging of rock cores, both for modelling purposes and for experimental implementation (Blunt et al., 2013; Cnudde and Boone, 2013; Wildenschild and Sheppard, 2013). One great advantage of this technique is that it has the potential, as recognised in the earliest work on micro-tomography by Flannery et al. (1987), "to study contained systems under conditions of temperature, pressure, and environment representative of process conditions". This is very attractive for the examination of the $scCO_2$–brine–rock system,

* Corresponding author at: Department of Earth Science and Engineering, South Kensington Campus, Imperial College London, SW7 2AZ, United Kingdom.
Tel.: +44 2075941359; fax: +44 2075947444.
E-mail address: m.andrew11@imperial.ac.uk (M. Andrew).

1750-5836
http://dx.doi.org/10.1016/j.ijggc.2013.12.018

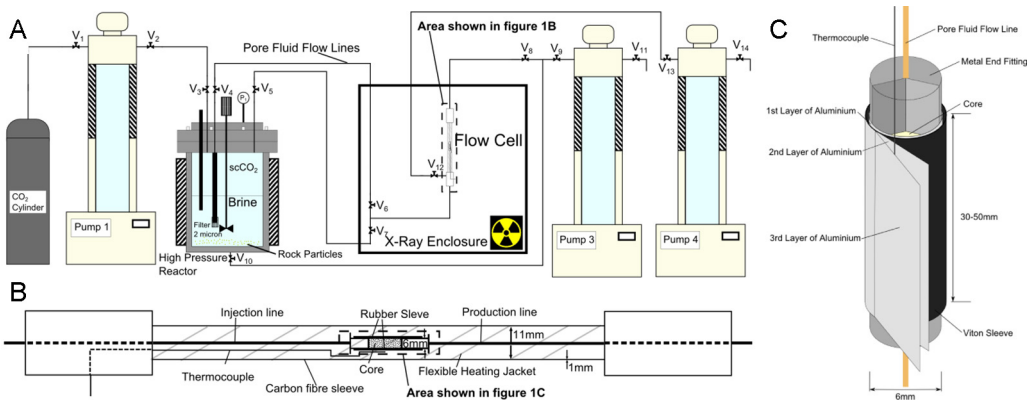

Fig. 1. Experimental apparatus. (A) The pumps used to control flow and the sitting of the flow cell within the μCT enclosure. (B) The detail of the flow cell and heating apparatus and the sitting of the core assembly. (C) Detail of the core assembly showing a triple wrap of aluminium around the core to prevent diffusive exchange across the Viton sleeve.

as the multi-phase flow behaviour of $scCO_2$ is highly dependent on thermo-physical properties, such as interfacial tension and contact angle, which are in turn a strong function of system conditions such as temperature, pressure and salinity (Espinoza and Santamarina, 2010; Li et al., 2012; Spiteri et al., 2008). The convolution of these variables with differences in rock structure and chemistry means that experiments in idealised pore structures (Chaudhary et al., 2013) and using analogue fluids (Karpyn et al., 2010; Wildenschild et al., 2011) may not be applicable to flow processes in the subsurface. Imaging multiple fluids at conditions representative of prospective CO_2 injection aquifer formations has, however, remained a challenge (Silin et al., 2011), with to date only three studies imaging real rocks under such conditions (Andrew et al., 2013a,b; Iglauer et al., 2011), and one study imaging simplified systems of bead packs and crushed glass (Chaudhary et al., 2013).

In our previous work (Andrew et al., 2013a,b) we have established a method to visualise $scCO_2$ and brine distributions within the pore space of Ketton limestone under reservoir conditions. Moreover, we demonstrated that at conditions of chemical equilibrium between fluid and rock phases, significant amounts of $scCO_2$ can be trapped by capillary forces. In this work, we expand on the results for a single carbonate and sandstone rock sample shown in (Andrew et al., 2013b), conducting high pressure – elevated temperature experiments to examine a wide suite of carbonate and sandstone rock types with different pore architectures. Furthermore, we compare images of multi-phase flow at in situ conditions to detailed topological analyses of the pore space to provide new insights into the relative importance of pore structure and mineralogy on the trapping process.

2. Methodology

2.1. Apparatus and sample preparation

The experimental apparatus is shown in Fig. 1. The imaging was performed using a Versa XRM-500 X-Ray Microscope (Zeiss X-Ray Microscopy, Pleasanton, CA, USA). The experiments were conducted on five different quarry samples; two sandstones (Bentheimer and Doddington), and three carbonates (Ketton, Mount Gambier and Estaillades). Details about each rock are provided in Table 1, while physical and chemical properties are given in Table 2.

The samples were drilled into cylindrical cores 6.5 mm in diameter and 30 mm to 50 mm in length. These cores were then placed within a fluoro-polymer elastomer (Viton) sleeve, which was attached to metal fittings connecting the core to the pore-fluid flow lines. This assembly was then placed within a high-temperature high-pressure Hassler type flow cell (Fig. 1B). To prevent diffusive $scCO_2$ exchange across the elastomer sleeve, the core assembly was wrapped three times in aluminium foil, once between the core and the sleeve, once between Viton sleeve and the thermocouple, and once on the outside of the thermocouple (Fig. 1C).

The challenge in imaging multiple phases at elevated pressures and temperatures is how to maintain such extreme conditions in a vessel both small enough to fit inside the μCT scanner with a large amount of geometric magnification, while being sufficiently X-ray transparent to allow for effective imaging. The solution to this lies in the central section of the core-holder, which is constructed of M55 carbon fibre. This is capable of maximum working pressures of 50 MPa with a vessel wall thickness of 1 mm, making it virtually transparent to X-rays. Sample stability during scanning is critical to the production of high quality images, as sample motion will cause blurring during the reconstruction process. The core-holder was clamped to the sample stage using a custom designed clamping system and attached to the rest of the flow apparatus using 1.59 mm diameter polyether ether ketone (PEEK) tubing (Kinesis, St. Neots, UK, Part Number: 1560xL). These flow lines were flexible, providing very little lateral load to the core-holder during image acquisition, which would cause sample motion.

Temperature in the flow-cell was maintained using an external Kapton insulated flexible heater (Omega Engineering, Manchester, UK, Model KH Series) connected to a custom built PID controller and thermocouple sitting in the confining annulus of the cell (Omega Engineering, Manchester, UK, Model: LMTSS-IM025U-300) between the second and third aluminium core wraps (Fig. 1C). By sitting the thermocouple on the exterior of the confining sleeve

Table 1
Basic details about each rock type.

Sample	Rock type	Geological group	Place of origin	Age/million years
Ketton	Carbonate	Upper Lincolnshire Limestone Member	Ketton, Rutland, UK	169–176
Mount Gambier	Carbonate	Heytesbury Group	Mount Gambier, Australia	15–38
Estaillades	Carbonate	Estaillade Formation	Oppède, France	22
Bentheimer	Sandstone	Bentheim Sandstone Member	Bad Bentheim, Germany	133–140
Doddington	Sandstone	Fell Sandstone Formation	Doddington, Northumberland, UK	343–339

Table 2
Basic petrophysical properties and chemical composition of each rock type. Chemical composition was found using X-ray diffraction.

Sample	Helium porosity	Permeability (m^2)	% Calcite	% Quartz	% Feldspar	% Clay
Ketton	0.2337[a]	2.807×10^{-12}[a]	99.1[a]	0.9[a]	0[a]	0[a]
Mount Gambier	0.552[a]	6.676×10^{-12}[a]	100[b]	0[b]	0[b]	0[b]
Estaillades	0.295[a]	1.490×10^{-13}[a]	97.9[a]	2.1[a]	0[a]	0[a]
Bentheimer	0.20[c]	1.875×10^{-12}[c]	0[b]	95[b]	4[b]	1[b]
Doddington	0.192[a]	1.038×10^{-12}[a]	0.2[a]	93.6[a]	1.7[a]	4.5[a]

[a] Analysis conducted at Weatherford Laboratories (East Grinsted, UK).
[b] Analysis conducted at the Natural History Museum (London, UK).
[c] Analysis conducted at Imperial College (London, UK).

right next to the core we obtain an accurate, reliable and stable reading of the pore-fluid temperature. The temperature was set at 50 °C and was seen to be constant to ±1 °C throughout the experiment. The salinity of the brine (7 wt% Potassium Iodide (KI)) was representative of aquifer salinities. KI was used as an ionic salt as it has a high atomic weight causing a high X-ray attenuation coefficient, allowing for it to be used as a contrast agent. The concentration was tuned so that the bulk attenuation coefficient of the brine was roughly intermediate between the rock and the $scCO_2$, easing the image segmentation process.

When $scCO_2$ is injected into a saline carbonate aquifer it will dissolve in the resident brine, forming highly reactive carbonic acid, which will in turn start to dissolve any calcite present. In order to remove reaction from the effects of multi-phase flow on residual saturation and ganglion dynamics, these processes have to be negated through creating equilibrium conditions representative of those far from the aquifer injection site. The brine was therefore pre-equilibrated with $scCO_2$ by vigorously mixing the two fluids together with small particles of the host rock using an entrainment stirrer in a heated reactor (Parr Instruments Co., IL, USA). For experiments on the two sandstone samples only the two fluid phases were mixed together.

High pressure syringe pumps were used to maintain pressure and control flow in the pore-space of the rock and in the reactor (Teledyne Isco, Lincoln, NE, USE, Model: 1000D), with a displacement resolution of 25.4 nl.

2.2. Injection strategy

Fluids were injected under conditions analogous to the "unsteady state" conditions used in larger scale core-flood experiments. Each experiment would consist of the following steps:

(1) The pressure and temperature in the reactor was raised to that desired for the pore fluid during the experiment (50 °C and 10 MPa), and was vigorously mixed.
(2) A confining pressure of 11 MPa was established within the cell, compressing the Viton sleeve around the core and the metal end-caps, preventing any fluid bypass.
(3) The pore space was filled with KI doped brine that had not been equilibrated with $scCO_2$. The temperature and pressure of the core was then raised to those within the reactor.
(4) More than 1000 pore volumes of equilibrated brine were flushed through the core to miscibly displace the unequilibrated brine, ensuring 100% initial brine saturation and create conditions in the core akin to the subsurface conditions in an aquifer at a point slightly ahead of the front of a $scCO_2$ plume.
(5) 1 ml (around 10 pore volumes) of $scCO_2$ was passed through the core at very low flow rates (1.67×10^{-9} m^3/s), ensuring a low capillary number of around 10^{-6}. 2D projections were continually taken in order to observe the point when $scCO_2$ displaces brine in the pore space.
(6) 1 ml (around 10 pore volumes) of equilibrated brine was passed though the core at the same low flow rate, causing $scCO_2$ to become trapped as a residual phase in the pore-space.

After step 5 or 6 scans were taken of the core to image either drainage or imbibition. For each rock type one experiment was run to image the initial saturation after drainage and five were run to image the residual saturation after imbibition. The initial non-wetting phase saturation was therefore only measured once, and was assumed to be the same for each experimental run in which imbibition was examined. This assumption was confirmed visually during each of the five experiments examining imbibition by comparing 2D projections taken during the drainage step (step 5) to those taken during the drainage step during the experiment where initial saturation was imaged. Only one rock core was used for each rock type in order to minimise confounding effects of structural heterogeneity within a single rock type.

2.3. Image acquisition

3D images were reconstructed using proprietary software on the Versa system. The voxel size (6.6 μm) was chosen so that the entire diameter of the core would fit into the field of view. To scan the entire length of the core while retaining a small voxel size, composite volumes were constructed by stitching together five overlapping sections, acquired sequentially. Each individual section consisted of around 1000^3 voxels. The stitching was done using software proprietary to the Versa XRM-500 system. Each section was reconstructed from a set of 400 projections, taking 15–20 min to acquire, meaning an entire composite volume took around 90 min. The image was then cropped to a cuboidal volume of around $900 \times 900 \times 3300$ voxels resulting in the image size of approximately $6 \times 6 \times 22$ mm; the quantitative analysis was restricted to this volume.

The dry scans were of 6 mm diameter cores that were drilled adjacent to the cores examined during wet scanning in order to minimise the effect of structural heterogeneity. They were then mounted on a kinematic stage and were single volumes reconstructed from a set of 1600 projections. They were processed and segmented using the same techniques as the wet scans, although the voxel sizes – between 6.2 and 3.9 μm – were smaller. To facilitate comparison between dry and wet scanning dry scanning results were reported in units equal in volume to the wet scanning voxel size (6.6 μm).

2.4. Image processing

After acquisition, the images were filtered using a non-local means edge preserving filter (Buades et al., 2005, 2008). The images were then segmented into two phases, with the $scCO_2$ being treated as one phase and the brine and the rock treated as the other phase. This was done as the segmentation of images containing a partial saturation of multiple fluids is significantly more difficult than the segmentation of dry images (Sheppard et al., 2004). As simple

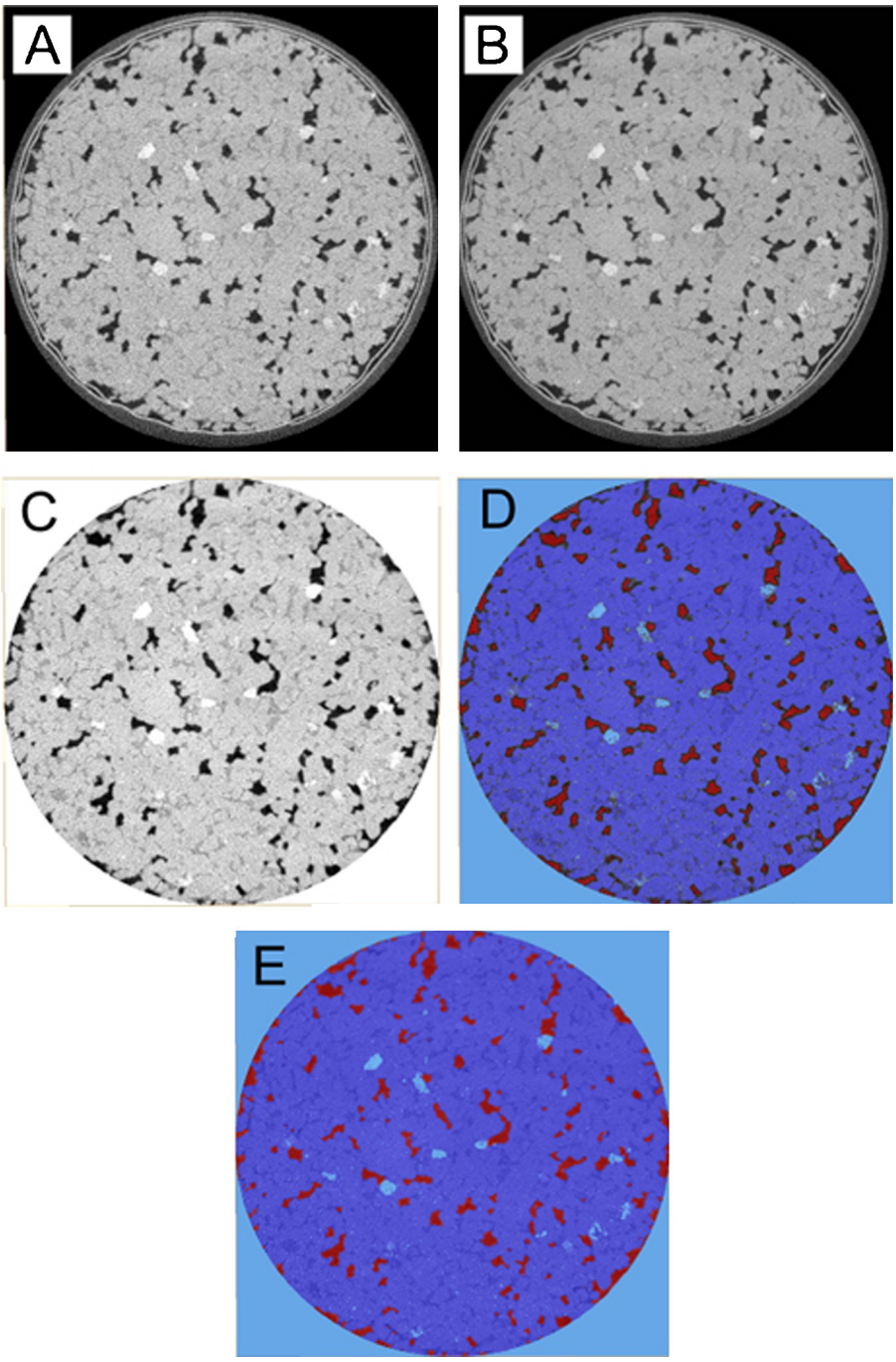

Fig. 2. The segmentation of a wet image consisted of five steps, shown here for Bentheimer sandstone. (A and B) The image was filtered using a non-local means edge preserving filter (Buades et al., 2005, 2008). (B and C) The image was cropped so only the core was in the field of view. (C and D) A seed was generated using 2D histogram (Jones et al., 2007). The red areas correspond to the $scCO_2$ portion of the seed and the dark blue areas to brine and grain, which are grouped together as a single phase. The light blue area corresponds to the area of the scan outside the core. (D and E) Each voxel outside the seeded areas was assigned to a phase using a watershed algorithm.

grey-scale segmentation is insufficient, segmentation using a watershed algorithm computed off a seed generated using a 2D histogram was performed (Jones et al., 2007). This eliminated much of the arbitrary voxel misidentification associated with simple histogram based segmentation. This image processing work flow is shown for Bentheimer in Fig. 2.

The segmented image was then analysed in 3D in order to identify and measure the volume of each unique disconnected ganglion, which was then labelled, as shown in Figs. 3–7. All this process was conducted within the Avizo Fire 8.0 (Visual Sciences Group, Burlington, MA, USA) and imageJ programs.

The apparent porosity as evaluated from the dry μCT images is shown in Table 3. For Bentheimer, Doddington and Mt Gambier this is similar to that obtained using helium porosimetry (Table 2); however for Estaillades and Ketton the apparent porosity is significantly smaller. This is due to the presence, in these rock types, of significant sub-resolution microporosity. These pores are apparent on mercury injection analysis performed separately and have high capillary entry pressures (>0.1 MPa) compared to the maximum possible capillary pressures generated during these experiments (<0.01 MPa), so are assumed to remain saturated with brine for the duration of the experiment.

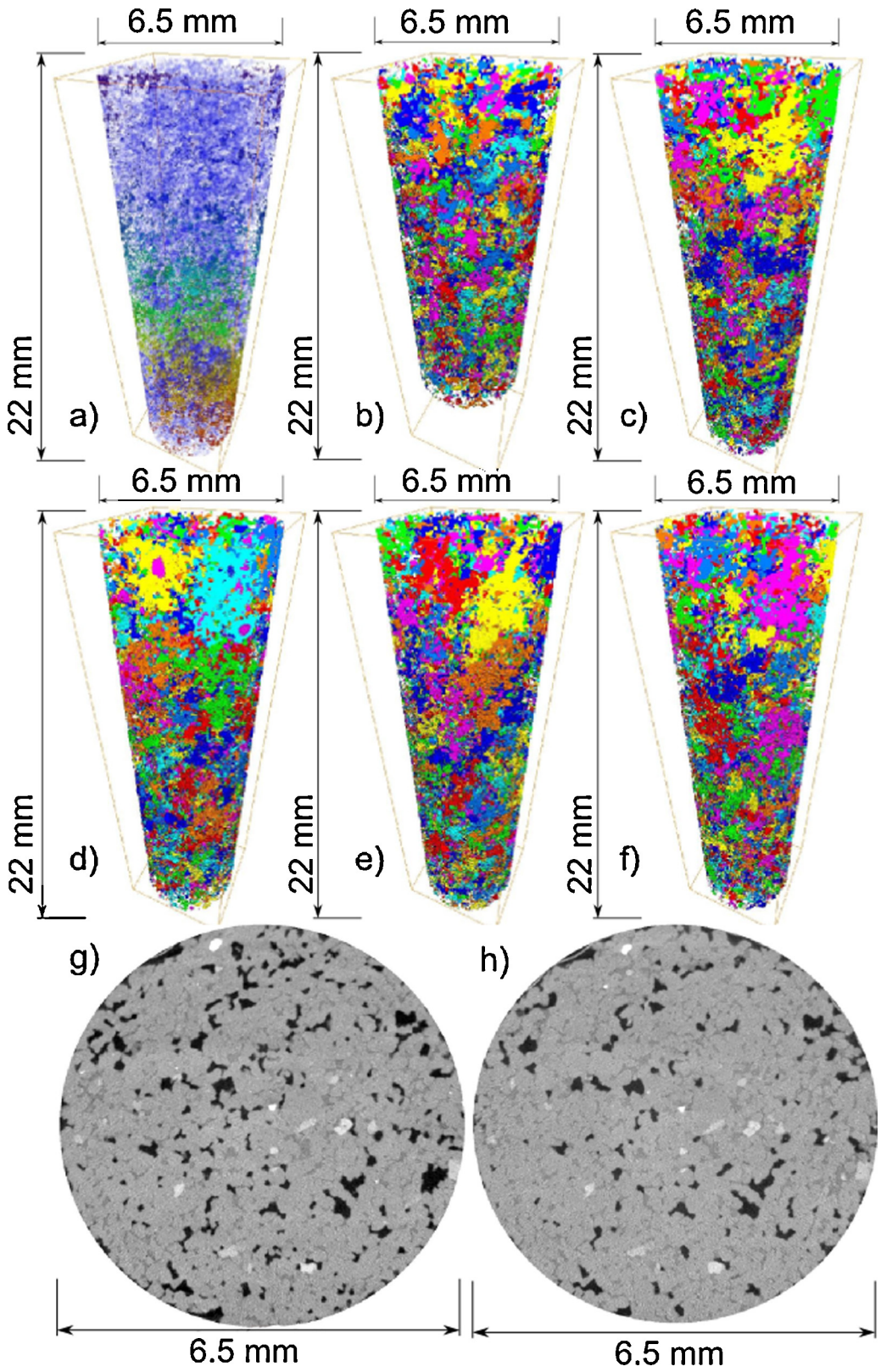

Fig. 3. Images of Bentheimer after drainage and imbibition. (A) A 3D rendering of the core after drainage where each non-wetting phase cluster is given a different colour. (B–F) A 3D rendering of the core after imbibition coloured as described for (A). The large range of colours indicates a poorly connected residual phase. (G) A cross-section of the core after drainage. (H) A cross-section of the core after imbibition.

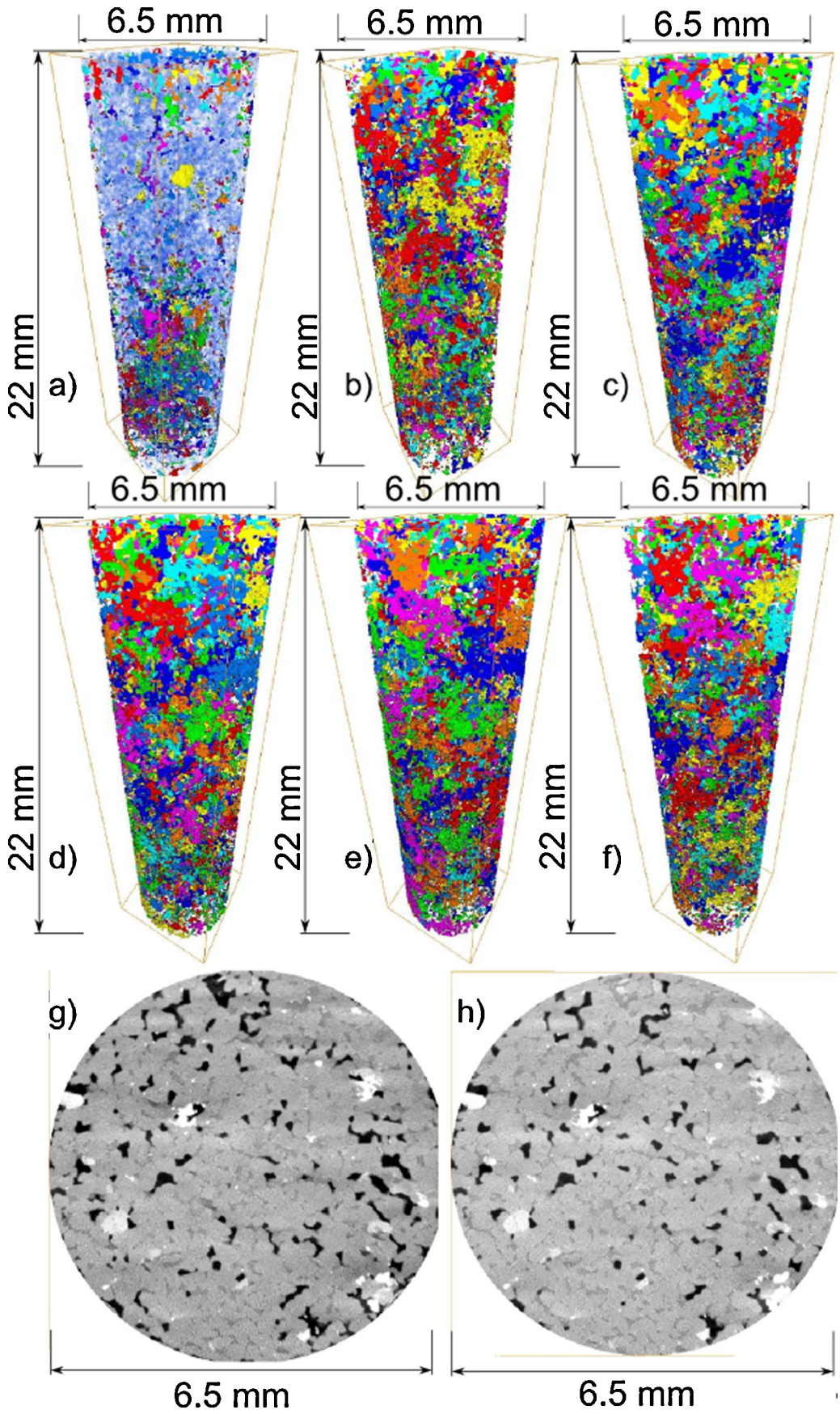

Fig. 4. Image of Doddington after drainage and imbibition. (A) A 3D rendering of the core after drainage where each non-wetting phase cluster is given a different colour. (B–F) A 3D rendering of the core after imbibition coloured as described for (A). The large range of colours indicates a poorly connected residual phase. (G) A cross-section of the core after drainage. (H) A cross-section of the core after imbibition.

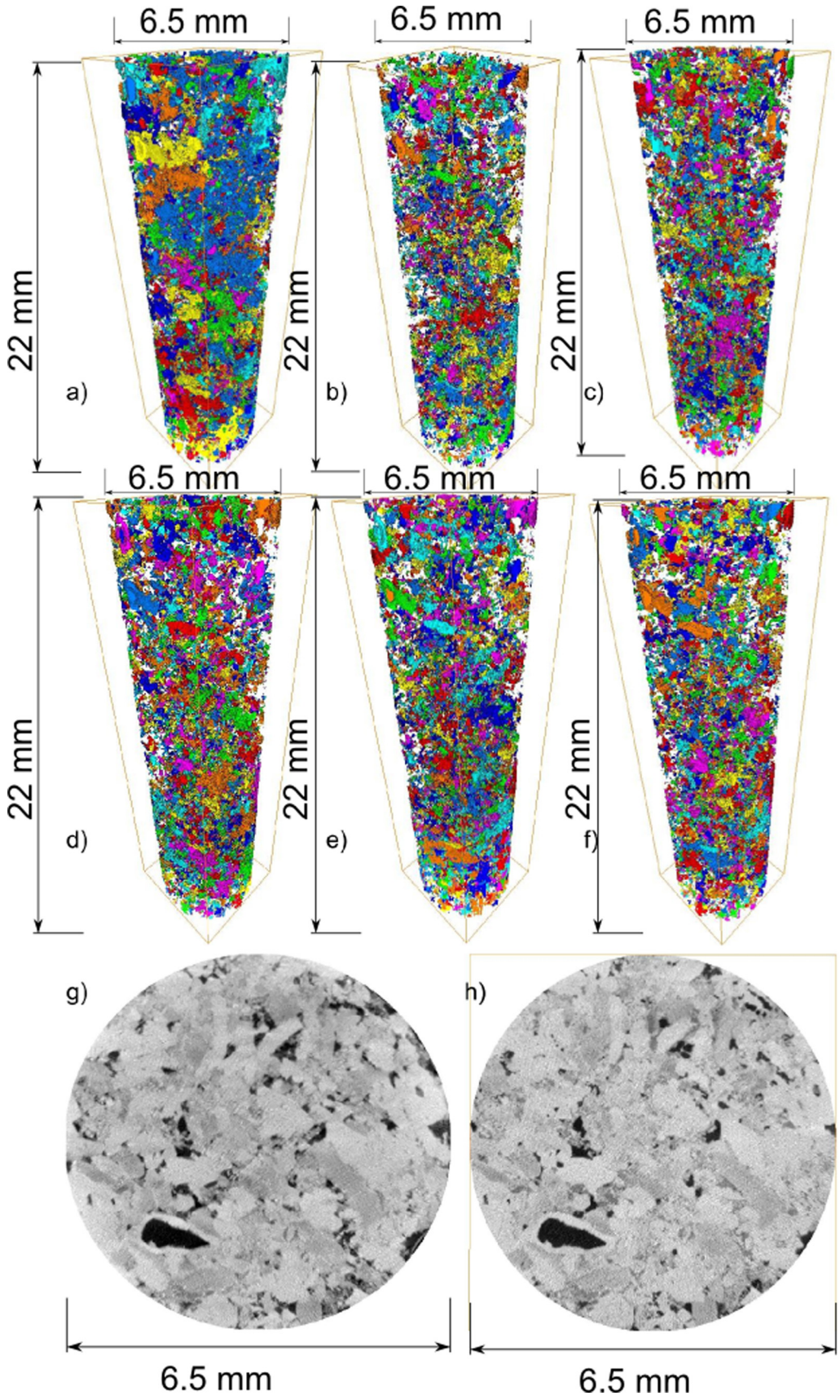

Fig. 5. Image of Estaillades after drainage and imbibition. (A) A 3D rendering of the core after drainage where each non-wetting phase cluster is given a different colour. (B–F) A 3D rendering of the core after imbibition coloured as described for (A). The large range of colours indicates a poorly connected residual phase. (G) A cross-section of the core after drainage. (H) A cross-section of the core after imbibition.

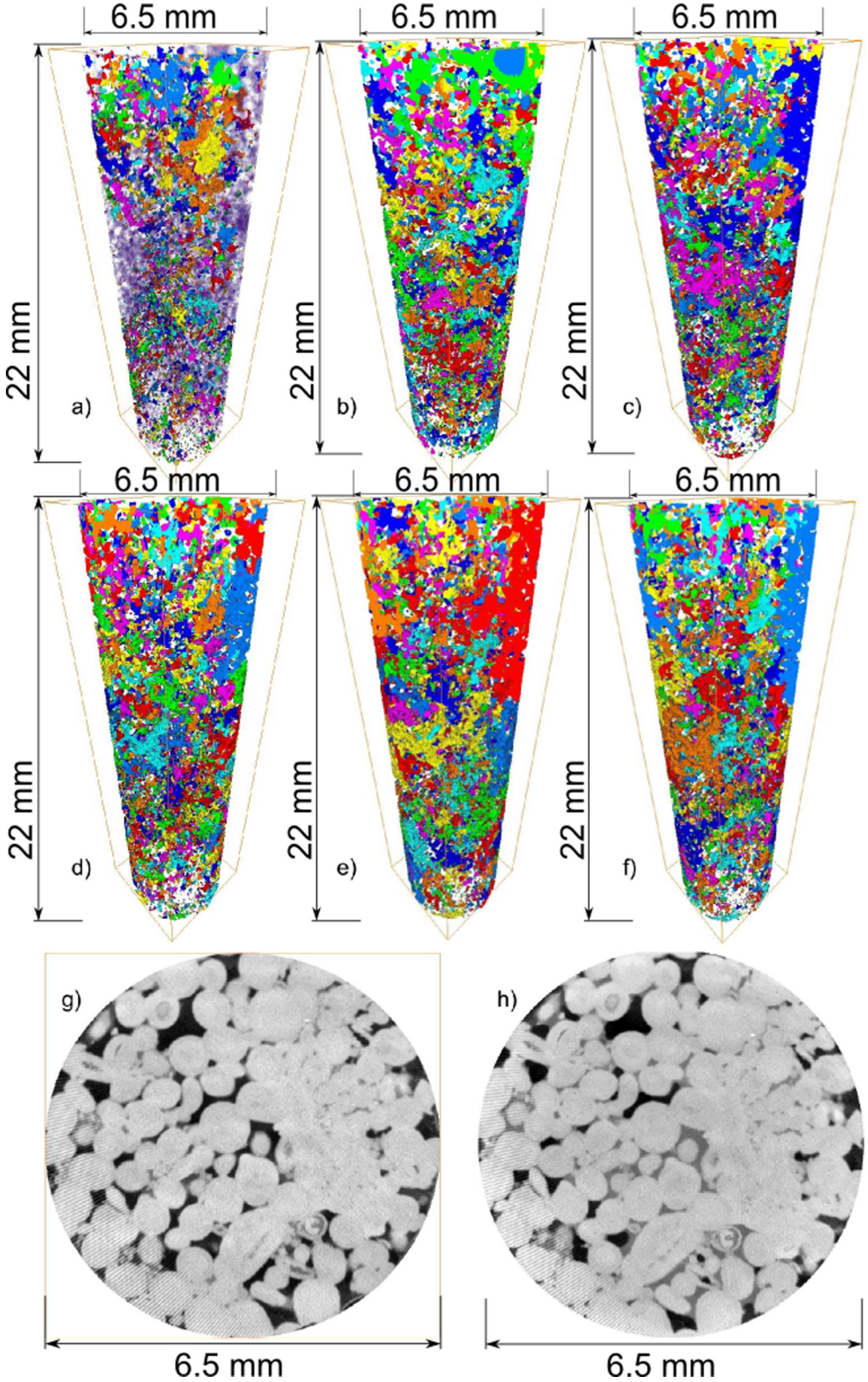

Fig. 6. Image of Ketton after drainage and imbibition. (A) A 3D rendering of the core after drainage where each non-wetting phase cluster is given a different colour. (B–F) A 3D rendering of the core after imbibition coloured as described for (A). The large range of colours indicates a poorly connected residual phase. (G) A cross-section of the core after drainage. (H) A cross-section of the core after imbibition.

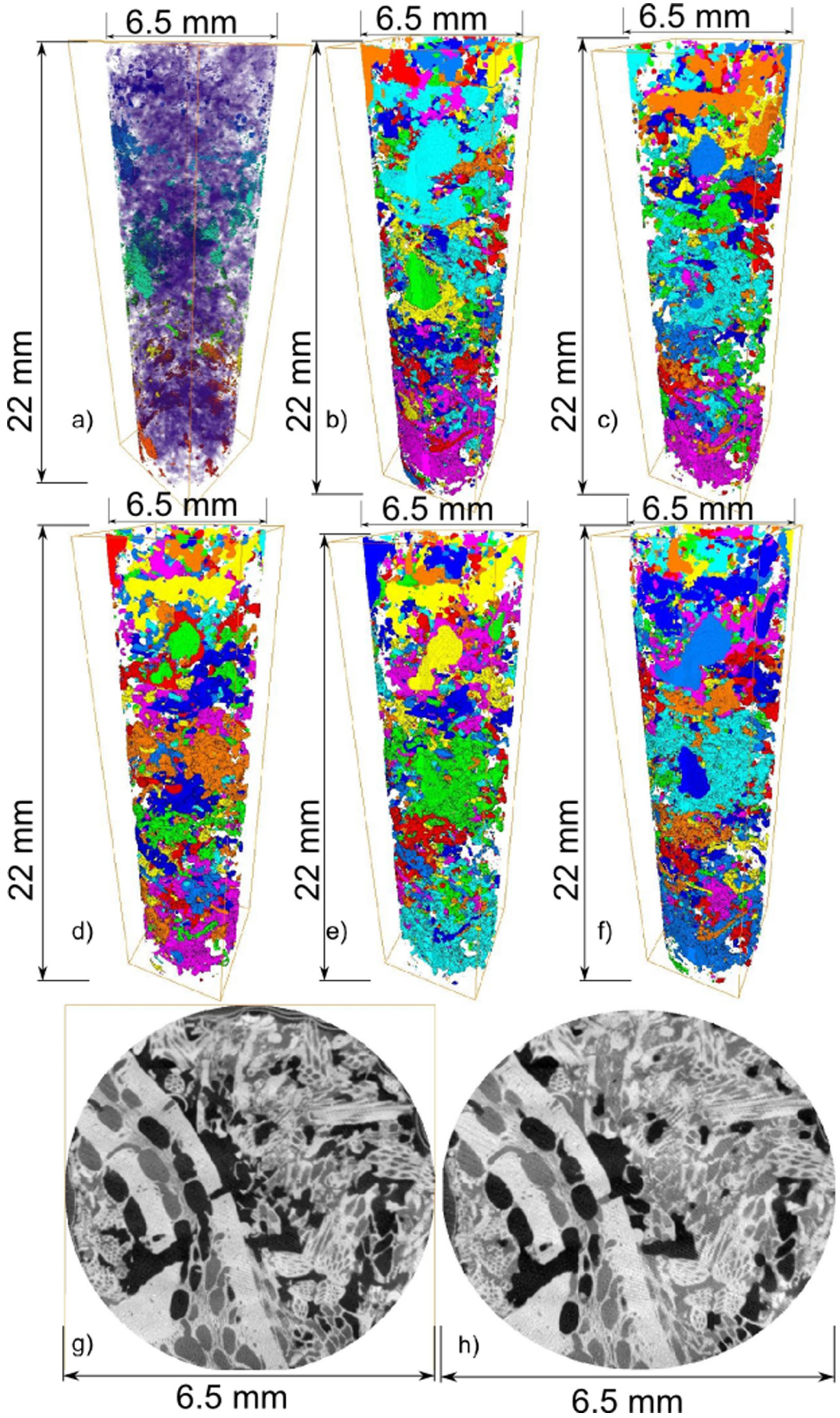

Fig. 7. Image of Mount Gambier after drainage and imbibition. (A) A 3D rendering of the core after drainage where each non-wetting phase cluster is given a different colour. (B–F) A 3D rendering of the core after imbibition coloured as described for (A). The large range of colours indicates a poorly connected residual phase. (G) A cross-section of the core after drainage. (H) A cross-section of the core after imbibition.

Table 3
Summary of the results of dry scanning and network extraction.

Sample	Voxel size (μm)	Apparent porosity	Helium porosity	Modal pore size (voxel^3)	Pore-volume weighted connectivity
Bentheimer	6.16	0.221	0.20[a]	413	6.92
Doddington	5.39	0.198	0.192[b]	577	5.68
Estaillades	4.60	0.097	0.295[b]	234	5.17
Ketton	4.44	0.129	0.2337[b]	1756	5.30
Mt Gambier	3.93	0.517	0.552[b]	1072	20.71

[a] Measured at Imperial College (London, UK).
[b] Measured at Weatherford Laboratories (East Grinsted, UK).

Pore networks were extracted from the dry scans by using a topological analysis of the pore space in which the largest voids are identified as pores by the method of maximal inscribed spheres (Dong and Blunt, 2009). Modal pore volumes were then found from this distribution by fitting a Gaussian distribution to the natural logarithm of the pore size distribution, as shown in Fig. 8. The pore-volume weighted connectivity for each sample was calculated by weighting the coordination number of a pore (the number of other pores connected to it) with its volume, then calculating an overall average. This was used as a metric of the connectivity of the pore space, as straight statistical averaging hides the impact of very large, very well connected pores to the overall connectivity. It corresponds to the average connectivity of a hypothetical volumetric element within the network model (Table 3). It can be seen from this analysis that Mount Gambier is much better connected than the other samples, as we might expect for a rock with such an extremely high porosity and permeability. The other two carbonates (Estaillades and Ketton) were slightly less connected than the two sandstones; Bentheimer was better connected than Doddington. These differences are much smaller, however, than that between Mount Gambier and all other samples. These results are summarised in Table 3.

3. Results and discussion

The segmented wet images were analysed by counting the number of voxels of residually trapped $scCO_2$ to find the proportion of the rock volume occupied by trapped $scCO_2$ – the capillary trapping capacity. This can then be converted to a residual saturation (S_r) by dividing this value by the porosity as obtained using helium porosimetry. In all rock types, significant proportions of $scCO_2$ were trapped as a residual phase. Sandstones tended to have higher residual saturations than carbonates, and higher capillary trapping capacities. The exception to this trend was Mt Gambier, which had an extremely high capillary trapping capacity, yet a rather low residual saturation due to the extremely high porosity and connectivity of this sample.

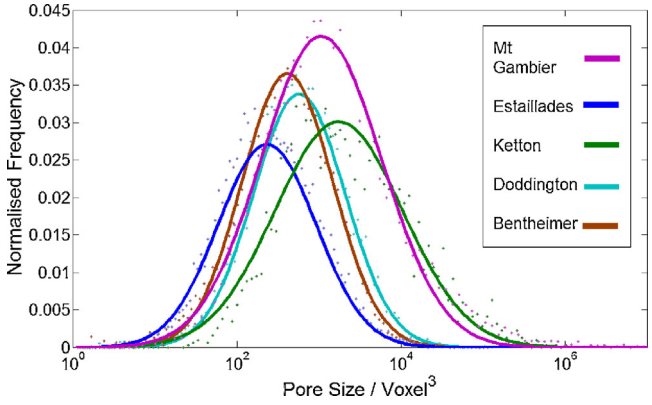

Fig. 8. Pore size distributions for each rock type. Each binned distribution was fitted using a logarithmic Gaussian distribution in order to find modal pore sizes (Table 3) which would be used as a lower cut-off for the ganglia size distributions. The pore size units are the same as used in Fig. 9.

The residual saturation in Ketton (0.203 ± 0.013; see Table 4) agrees with that found in previous μCT studies (0.19 ± 0.03) (Andrew et al., 2013a) using similar experimental apparatus. Larger core-scale studies of residual trapping in this rock type showed a lower residual saturation of 0.137 ± 0.012 (El-Maghraby, 2013; El-Maghraby and Blunt, 2013). Data was not available for direct comparison with the other samples; however, the behaviour of $scCO_2$ and brine has been studied in Berea, a consolidated sandstone similar to Doddington and Bentheimer. A residual saturation of 0.25 was found at the core scale (Pentland et al., 2011), and 0.249 at the pore scale (Iglauer et al., 2011). This compares to 0.320 ± 0.010 in Bentheimer and 0.33 ± 0.04 in Doddington in this study.

The variation of residual saturation between carbonates (with an average of 0.19) and sandstones (with an average of 0.325) can be explained by variations in the initial saturation (S_i), variations in the porosity and variations in the ratio of microporosity to macroporosity of each sample. If, instead, we look at the efficiency of trapping (the fraction of the initial $scCO_2$ which is trapped in place after waterflood; S_r/S_i) then we find much less variation (0.65–0.71) over the rock types. The sandstones showed a slightly larger capillary trapping efficiency (with Doddington and Bentheimer showing efficiencies of 0.681 and 0.706 respectively) to the carbonates (with Mount Gambier, Estaillades and Ketton showing efficiencies of 0.662, 0.646 and 0.653 respectively). This compares to a capillary trapping efficiency of 0.50 seen in larger core-scale experiments in Berea sandstone (Pentland et al., 2011). Traditional trapping models, such as Land's model, relate S_r to S_i and the maximum non-wetting phase saturation ($S_{i,\max}$) and the trapping seen at that saturation ($S_{r,\max}$) (Land, 1968). In the Land model the efficiency of trapping can be expressed as:

$$\frac{S_r}{S_i} = \frac{1}{1 + CS_i} \tag{1}$$

where C is the Land coefficient, defined as:

$$C = \frac{1}{S_{r,\max}} - \frac{1}{S_{i,\max}} \tag{2}$$

Our S_i varies by roughly factor of 2 (with S_i ranging from 0.238 for Estaillades to 0.488 for Doddington) and, although the Land coefficient for the same fluid system can vary significantly across rocks of different permeability (Spiteri and Juanes, 2006); we do not see much difference in trapping efficiency in our experiments. The micro-flow cell seems to show more trapping than seen in larger scale experiments, possibly due to the limited flow domain preventing displacement of some $scCO_2$ that would be mobile in a larger system.

The ingress of brine into a $scCO_2$ saturated core is an imbibition process where a wetting fluid (brine) invades each pore, displacing non wetting fluid ($scCO_2$). In a strongly water-wet rock we expect the water to fill areas of the pore space in order of size (Roof,

Table 4
Summary of results for trapped saturation. The largest ganglion contribution refers to the fraction of the total residual $scCO_2$ residing in the largest unique ganglion.

Sample	Volume (voxel)	Volume (mm)	Initial saturation	Residual saturation	Capillary trapping capacity	S_r/S_i	Largest ganglion contribution	Fitted Fisher exponent
Bentheimer	927 × 908 × 3305	6.078 × 5.954 × 21.67	0.453	0.320 ± 0.010	0.070 ± 0.002	0.706	0.06 ± 0.06	2.106 ± 0.011
Doddington	916 × 906 × 3306	6.006 × 5.941 × 21.68	0.488	0.33 ± 0.04	0.064 ± 0.008	0.681	0.06 ± 0.06	2.17 ± 0.03
Estaillades	927 × 904 × 3304	6.078 × 5.928 × 21.66	0.238	0.155 ± 0.005	0.0458 ± 0.0014	0.646	0.0137 ± 0.0011	2.280 ± 0.013
Ketton	900 × 877 × 3314	5.901 × 5.750 × 21.73	0.313	0.203 ± 0.013	0.047 ± 0.003	0.653	0.05 ± 0.02	2.287 ± 0.009
Mt Gambier	891 × 888 × 3296	5.842 × 5.823 × 21.61	0.320	0.212 ± 0.009	0.116 ± 0.005	0.662	0.260 ± 0.013	1.834 ± 0.009

1970), trapping disconnected ganglia in the process called snap-off. This process should be percolation like (Dias and Wilkinson, 1986) so predictions can be made about the size distribution of the isolated clusters. The number n of clusters of volume s (measured in voxels) should scale as $n(s) \sim s^{-\tau}$, where τ is the Fisher exponent (Fisher, 1967). Network modelling has shown that in three-dimensional cubic regular lattices the value of this exponent is around $\tau = 2.189$ (Lorenz and Ziff, 1998). This scaling exponent is useful when assessing storage security, as the higher the value of the exponent the higher the ratio of small ganglia to large ganglia. This increases storage security as small ganglia are less easy to mobilise by viscous or gravitational forces; they also present a relatively larger surface area for dissolution and reaction.

In real systems the distribution of ganglia sizes will be affected by two other effects; clusters can be neither smaller than a single pore, nor larger than the system size. The modal pore size, as found by the topological analysis of the pore space (Fig. 8) was for each sample between 2×10^2 voxel^3 and 2×10^3 voxel^3. As a result 10^3 voxel^3 was used as a lower cut-off for ganglion size. Lowering the effect of the upper cut-off by increasing system size was the motivation behind examining stitched volumes of multiple scans.

One way to assess the effect of the system size on overall behaviour (or how close one is to the representative elementary volume, or REV, defined as the minimum volume for which a volume increase does not change system behaviour) is to look at the contribution that the largest unique ganglion makes to the overall residual saturation. If the total trapped volume is an order of magnitude or more larger than the largest single ganglion, we can be fairly confident that all ganglia are statistically well represented and the system size (approximately the same for each rock type) is above the REV. This is the case for all rock types apart from Mount Gambier (Table 4), where the extremely high porosity and connectivity of the pore-space (as discussed above) prevents complete trapping for small blobs and encourages the formation of extremely large ganglia. In this case 26% of the total residual $scCO_2$ resides in the largest single ganglion, contributing 0.055 ± 0.003 to the residual saturation. These results are different to findings for trapping in a bead pack for an oil–brine–rock system (Georgiadis et al., 2011), where the contribution of the largest ganglion was much more significant, underlining the importance of experiments at representative pressures and temperatures when assessing problems pertaining to $scCO_2$ storage.

The impact of system size, however, can never be totally ruled out, at least in the direction perpendicular to flow. The largest ganglia may therefore still be constrained both by this effect and by potential capillary end effects.

One natural way of extracting the Fisher exponent from real data is to plot the binned quantity, as defined by Dias and Wilkinson (1986).

$$N_s = \sum_{s'=s}^{2s-1} n_s \tag{3}$$

which should scale as:

$$N_s \sim s^{-(\tau-1)} \tag{4}$$

This is then plotted on a log–log plot as a function of s (Fig. 9), showing power-law behaviour for large ganglia, but an under-representation of smaller ganglia compared to the power law model. All the experiments for each rock type were put into a single graph. The exponents were then calculated by excluding ganglia smaller than 10^5 voxels (approximately the start of the power-law behaviour) and performing Levenberg–Marquardt regression (Levenberg, 1944; Marquardt, 1963) using a least absolute residual robust fitting algorithm (Holland and Welsch, 1977; Huber, 1981).

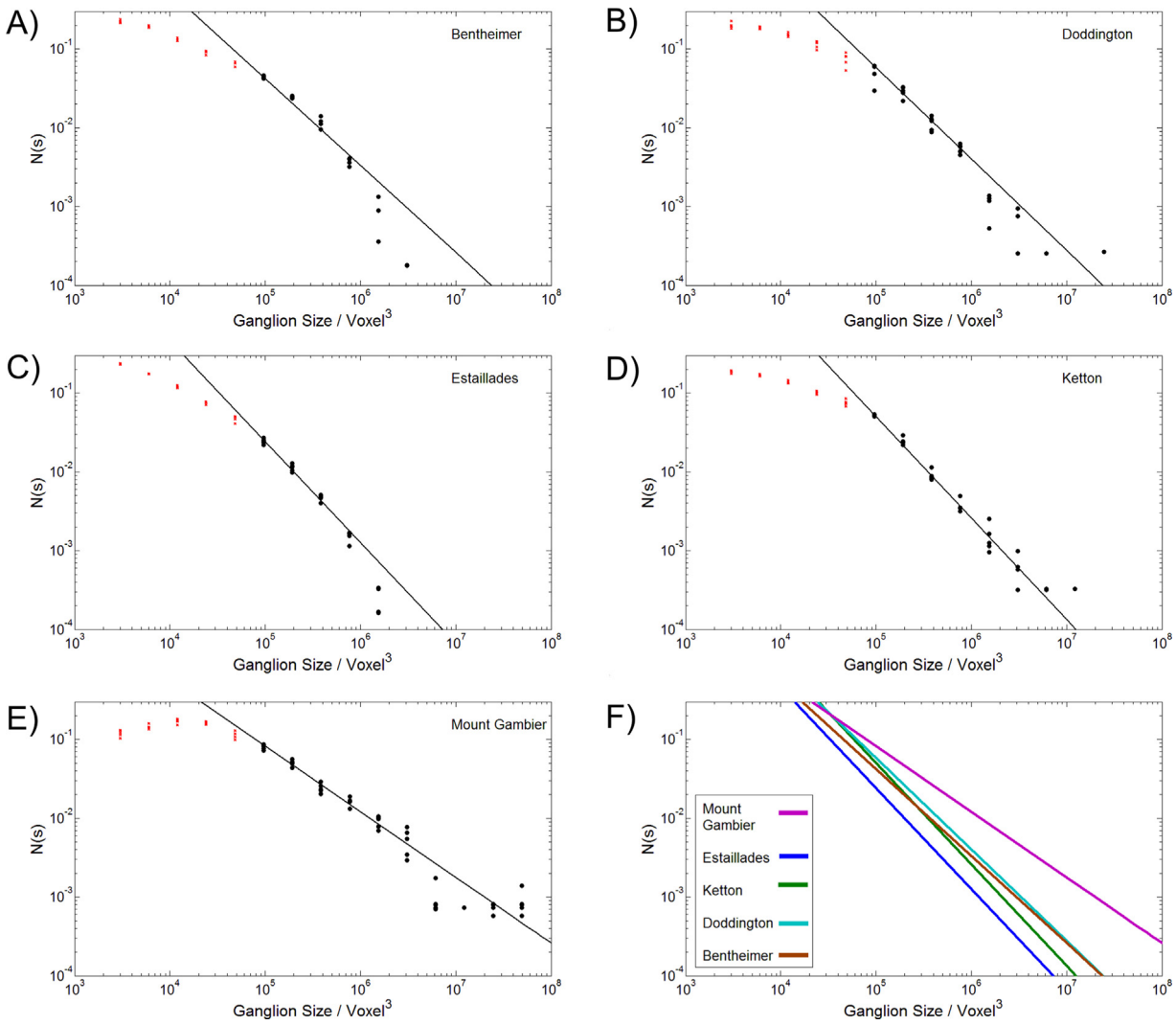

Fig. 9. Ganglia size distribution (N_s), Eq. (1), for all rock types. (A) Bentheimer, (B) Doddington, (C) Estaillades, (D) Ketton, and (E) Mount Gambier. (F) Shows the fit lines all plotted together. Red data points are excluded from the percolation analysis.

This was performed using a commercial software package (MATLAB R2013a, The MathWorks Inc., Natick, MA, 2013).

The under-representation of smaller ganglia in all sample types may be explained by the fact that the $scCO_2$–brine–rock system is not strongly water-wet (Espinoza and Santamarina, 2010; Jung and Wan, 2008; Kim et al., 2012; Yang et al., 2008). This means that the exact nature of local pore filling and trapping may not be strictly percolation like, as cooperative pore filling or piston-like displacement may become more or less important compared to snap-off (Valvatne and Blunt, 2004). Larger (above 10^5 voxel^3) ganglia, however, see the system as a whole, averaging out local heterogeneity in the pore filling mechanism, so at this scale the trapping can only be fundamentally controlled by the hierarchy of pore sizes, and so the behaviour is percolation like. These results are summarised in Table 4.

For all samples other than Mount Gambier, the calculated exponent fell in the range between 2.1 and 2.3, close to the theoretical value in three dimensions of 2.189. Mount Gambier had a significantly smaller Fisher exponent (1.83) which may be due to the extremely high connectivity of the pore space. This may lead to an inhibition of snap-off that disconnects the non-wetting phase, as piston like displacements or cooperative filling may come to dominate in these unusual pore geometries. During the dynamic imbibition process non-wetting ganglia in this pore-space will be substantially better connected, making it more difficult for wetting phase bypass and snap-off to strand regions of the CO_2 completely. The other carbonates have a slightly higher apparent Fisher exponent than the sandstones. This could, in turn, be explained by

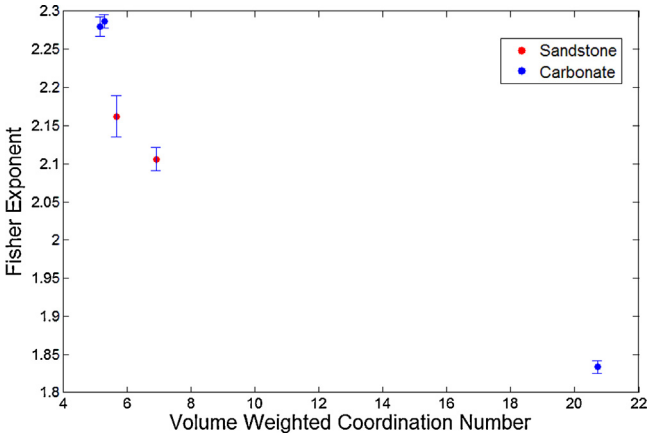

Fig. 10. The correlation of pore-volume weighted connectivity with Fisher exponent.

their slightly lower coordination numbers, as a greater proportion of the $scCO_2$ will reside in poorly connected portions of the pore space, which inhibit piston-like displacement compared to snap-off. Indeed there seems to be a general negative correlation between the pore-space connectivity and the fitted Fisher exponent (Fig. 10). The trapping efficiency of each rock type (S_r/S_i) is, however, similar – in the range 0.65–0.71 – meaning that the overall trapping behaviour appears to be fairly insensitive to pore structure.

More generally these results confirm conclusions in larger core-flood experiments (Akbarabadi and Piri, 2013; El-Maghraby, 2013; El-Maghraby and Blunt, 2013; Pentland et al., 2011) that $scCO_2$ acts as the non-wetting phase in carbonates and sandstones, while brine acts as the wetting phase. It also shows that in the $scCO_2$–brine–rock system differences in rock chemistry (at least under conditions of chemical equilibrium) matter less to the overall ganglion dynamics than differences in pore structure and connectivity. Significant residual saturations were observed in all samples, with two-thirds of the initial saturation trapped in all cases, indicating that residual trapping is a viable local trapping mechanism in a wide range of rock types.

4. Conclusions

We have non-invasively imaged multiple fluid phases ($scCO_2$ and brine) at high resolution (voxel size 6.6 μm) at pressures and temperatures representative of prospective subsurface storage sites in the pore-space of a suite of carbonate and sandstone rocks. In all cases, after brine injection significant proportions of the $scCO_2$ were trapped as a residual phase in clusters with sizes ranging over five orders of magnitude. In each case clusters larger than around 10^5 voxel^3 obeyed power law distributions consistent with percolation theory. Well-connected pore-spaces tended to have more large clusters relative to small clusters, and vice versa. The chemical composition of the rock had, however, comparatively little effect on the size distribution. This is encouraging for CCS, indicating that residual trapping can contribute to storage security for a wide range of rock types and compositions.

This experimental technique is easily applicable to other systems, and future work could study, at the pore scale, a wide variety of single phase and multiphase flow problems at conditions representative of subsurface aquifers, oil and gas fields and other deep geological systems.

Acknowledgments

We gratefully acknowledge funding from the Qatar Carbonates and Carbon Storage Research Centre (QCCSRC), provided jointly by Qatar Petroleum, Shell, and the Qatar Science & Technology Park, and the Imperial College Consortium on Pore-Scale Modelling.

References

Akbarabadi, M., Piri, M., 2013. Relative permeability hysteresis and capillary trapping characteristics of supercritical CO_2/brine systems: an experimental study at reservoir conditions. Advances in Water Resources 52, 190–206, http://dx.doi.org/10.1016/j.advwatres.2012.06.014.

Andrew, M.G., Bijeljic, B., Blunt, M.J., 2013a. Pore-scale imaging of geological carbon dioxide storage under in situ conditions. Geophysical Research Letters 40, 3915–3918.

Andrew, M.G., Blunt, M.J., Bijeljic, B.,2013b. Reservoir-condition pore-scale imaging of supercritical carbon dioxide. In: SPE 166498, SPE Annual Technical Conference and Exhibition. SPE International, New Orleans, LA, USA.

Bachu, S., 2008. CO_2 storage in geological media: role, means, status and barriers to deployment. Progress in Energy and Combustion Science 34, 254–273, http://dx.doi.org/10.1016/j.pecs.2007.10.001.

Blunt, M.J., Bijeljic, B., Dong, H., Gharbi, O., Iglauer, S., Mostaghimi, P., Paluszny, A., Pentland, C.H., 2013. Pore-scale imaging and modelling. Advances in Water Resources 51, 197–216, http://dx.doi.org/10.1016/j.advwatres.2012.03.003.

Buades, A., Coll, B., Morel, J.-M., 2005. A non-local algorithm for image denoising. Computer Vision and Pattern Recognition, http://dx.doi.org/10.1109/CVPR.2005.38.

Buades, A., Coll, B., Morel, J.-M., 2008. Nonlocal image and movie denoising. International Journal of Computer Vision 76, 123–139, http://dx.doi.org/10.1007/s11263-007-0052-1.

Chaudhary, K., Cardenas, M.B., Wolfe, W.W., Maisano, J.A., Ketcham, R.A., Bennet, P.C., 2013. Pore-scale trapping of supercritical CO_2 and the role of grain wettability and shape. Geophysical Research Letters 40, 1–5, http://dx.doi.org/10.1002/grl.50658.

Cnudde, V., Boone, M.N., 2013. High-resolution X-ray computed tomography in geosciences: a review of the current technology and applications. Earth-Science Reviews 123, 1–17, http://dx.doi.org/10.1016/j.earscirev.2013.04.003.

Dias, M.M., Wilkinson, D., 1986. Percolation with trapping. Journal of Physics A: Mathematical and General 19, 3131–3146, http://dx.doi.org/10.1088/0305-4470/19/15/034.

Dong, H., Blunt, M.J., 2009. Pore-network extraction from micro-computerized-tomography images. Physical Review E 80, 036307, http://dx.doi.org/10.1103/PhysRevE.80.036307.

El-Maghraby, R., 2013. Measurements of CO_2 Trapping in Carbonate and Sandstone Rocks, Earth Science and Engineering. Imperial College, London.

El-Maghraby, R.M., Blunt, M.J., 2013. Residual CO_2 trapping in Indiana limestone. Environmental Science and Technology 47, 227–233, http://dx.doi.org/10.1021/es304166u.

Ennis-King, J., Paterson, L., 2002. Engineering aspects of geological sequestration of carbon dioxide. In: SPE 77809, Proceedings of the Asia Pacific Oil and Gas Conference and Exhibition, http://dx.doi.org/10.2523/77809-MS.

Espinoza, D.N., Santamarina, J.C., 2010. Water–CO_2–mineral systems: interfacial tension, contact angle, and diffusion-Implications to CO_2 geological storage. Water Resources Research, 46, http://dx.doi.org/10.1029/2009WR008634.

Fisher, M.E., 1967. The theory of equilibrium critical phenomena. Reports on Progress in Physics 30, 615, http://dx.doi.org/10.1088/0034-4885/30/2/306.

Flannery, B.P., Deckman, H.W., Roberge, W.G., D'Amico, K.L., 1987. Three-dimensional X-ray microtomography. Science 237, 1439–1444, http://dx.doi.org/10.1126/science.237.4821.1439.

Georgiadis, A., Berg, S., Maitland, G., Ott, H., 2011. Pore-scale micro-CT imaging: cluster size distribution during drainage and imbibition. In: SCA2011-59. Proceedings of the International Symposium of the Society of Core Analysts.

Hawkes, C., Mclellan, P., Bachu, S., 2005. Geomechanical factors affecting geological storage of CO_2 in depleted oil and gas reservoirs. Journal of Canadian Petroleum Technology 44, 52–61, http://dx.doi.org/10.2118/05-10-05.

Holland, P.W., Welsch, R.E., 1977. Robust regression using iteratively reweighted least-squares. Communications in Statistics: Theory and Methods 6, 813–827, http://dx.doi.org/10.1080/03610927708827533.

Huber, P.J., 1981. Robust Statistics. John Wiley & Sons, Inc., New York.

Iglauer, S., Paluszny, A., Pentland, C.H., Blunt, M.J., 2011. Residual CO_2 imaged with X-ray micro-tomography. Geophysical Research Letters, 38, http://dx.doi.org/10.1029/2011GL049680.

IPCC, 2007. Contribution of Working Group III to the fourth assessment report of the intergovernmental panel on climate change. In: Metz, B., Davidson, O.R., Bosch, P.R., Dave, R., Meyer, L.A. (Eds.), IPCC Fourth Assessment Report: Climate Change 2007. IPCC, Cambridge, UK/New York, NY, USA.

Jatsi, J.K., Jesion, G., Feldkamp, L., 1993. Microscopic imaging of porous media with X-ray computer tomography. In: SPE 20495. SPE Formation Evaluation, pp. 189–193, http://dx.doi.org/10.2118/20495-PA.

Jones, A.C., Arns, C.H., Sheppard, A.P., Hutmacher, D.W., Milthorpe, B.K., Knackstedt, M.A., 2007. Assessment of bone ingrowth into porous biomaterials using MICRO-CT. Biomaterials 28, 2491–2504, http://dx.doi.org/10.1016/j.biomaterials.2007.01.046 (Imaging Techniques for Biomaterials Characterization).

Jung, J., Wan, J., 2008. Supercritical CO_2 and ionic strength effects on wettability of silica surfaces: equilibrium contact angle measurements. Energy and Fuels 26, 6053–6059, http://dx.doi.org/10.1021/ef300913t.

Karpyn, Z.T., Piri, M., Singh, G., 2010. Experimental investigation of trapped oil clusters in a water-wet bead pack using X-ray microtomography. Water Resources Research, 46, http://dx.doi.org/10.1029/2008WR007539.

Kim, Y., Wan, J., Kneafsey, T.J., Tokunaga, T.K., 2012. Dewetting of silica surfaces upon reactions with supercritical CO_2 and brine: pore-scale studies in micromodels. Environmental Science and Technology 46, 4228–4235, http://dx.doi.org/10.1021/es204096w.

Lackner, K.S., 2003. Climate change: a guide to CO_2 sequestration. Science 300, 1677–1678, http://dx.doi.org/10.1126/science.1079033.

Land, C.S., 1968. Calculation of imbibition relative permeability for two- and three-phase flow from rock properties. Society of Petroleum Engineers Journal: Transactions of the AIME 243 (June), 149–156.

Levenberg, K., 1944. A method for the solution of certain non-linear problems in least squares. Quarterly Journal of Applied Mathematics 2, 164–168.

Li, X., Boek, E., Maitland, G., Trusler, J.P.M., 2012. Interfacial tension of (brines + CO_2): (0.864 NaCl + 0.136 KCl) at temperatures between (298 and 448) K, pressures between (2 and 50) MPa, and total molalities of (1 to 5) mol/kg. Journal of Chemical and Engineering Data 57, 1078–1088, http://dx.doi.org/10.1021/je201062.

Lin, H., Fujii, T., Takisawa, R., Takahashi, T., Hashida, T., 2007. Experimental evaluation of interactions in supercritical CO_2/water/rock minerals system under geologic CO_2 sequestration conditions. Journal of Materials Science 43, 2307–2315, http://dx.doi.org/10.1007/s10853-007-2029-4.

Lorenz, C.D., Ziff, R.M., 1998. Precise determination of the bond percolation thresholds and finite-size scaling corrections for the sc, fcc and bcc lattices. Physical Review E 57, 230–236, http://dx.doi.org/10.1103/PhysRevE.57.230.

Marquardt, D.W., 1963. An algorithm for least-squares estimation of nonlinear parameters. Journal of the Society for Industrial and Applied Mathematics 11, 431–441.

Pentland, C.H., El-Maghraby, R., Iglauer, S., Blunt, M.J., 2011. Measurements of the capillary trapping of super-critical carbon dioxide in Berea sandstone. Geophysical Research Letters 38, 4.

Qi, R., LaForce, T.C., Blunt, M.J., 2009. Design of carbon dioxide storage in aquifers. International Journal of Greenhouse Gas Control 3, 195–205, http://dx.doi.org/10.1016/j.ijggc.2008.08.004.

Roof, J.G., 1970. Snap-off of oil droplets in water-wet pores. SPE Journal 10, 85–90, http://dx.doi.org/10.2118/2504-PA.

Sheppard, A.P., Sok, R.M., Averdunk, H., 2004. Techniques for image enhancement and segmentation of tomographic images of porous materials. Physica A 339, 145–151, http://dx.doi.org/10.1016/j.physa.2004.03.057.

Silin, D., Tomutsa, L., Benson, S.M., Patzek, T.W., 2011. Microtomography and pore-scale modeling of two-phase fluid distribution. Transport in Porous Media 86, 495–515.

Spiteri, E.J., Juanes, R., 2006. Impact of relative permeability hysteresis on the numerical simulation of WAG injection. Journal of Petroleum Science and Engineering 50, 115–139, http://dx.doi.org/10.1016/j.petrol.2005.09.004.

Spiteri, E.J., Juanes, R., Blunt, M.J., Orr Jr., F.M., 2008. A new model of trapping and relative permeability hysteresis for all wettability characteristics. SPE Journal 13, 277–288, http://dx.doi.org/10.2118/96448-PA.

Valvatne, P.H., Blunt, M.J., 2004. Predictive pore-scale modeling of two-phase flow in mixed wet media. Water Resources Research, 40.

Wildenschild, D., Armstrong, R.T., Herring, A.L., Young, I.M., Carey, J.W., 2011. Exploring capillary trapping efficiency as a function of interfacial tension, viscosity, and flow rate. Energy Procedia 4, 4945–4952, http://dx.doi.org/10.1016/j.egypro.2011.02.464.

Wildenschild, D., Sheppard, A.P., 2013. X-ray imaging and analysis techniques for quantifying pore-scale structure and processes in subsurface porous medium systems. Advances in Water Resources 51, 217–246, http://dx.doi.org/10.1016/j.advwatres.2012.07.018.

Yang, D., Gu, Y., Tontiwachwuthikul, P., 2008. Wettability determination of the reservoir brine–reservoir rock system with dissolution of CO_2 at high pressures and elevated temperatures. Energy and Fuels 22, 504–509, http://dx.doi.org/10.1021/ef700383x.